Title	Effects of several types of biomass fuels on the yield, nanostructure and reactivity of soot from fast pyrolysis at high temperatures
Author(s)	Trubetskaya, Anna; Jensen, Peter Arendt; Jensen, Anker Degn; Garcia Llamas, Angel David; Umeki, Kentaro; Gardini, Diego; Kling, Jens; Bates, Richard B.; Glarborg, Peter
Publication Date	2016-03-24
Publication Information	Trubetskaya, A., Jensen, P. A., Jensen, A. D., Garcia Llamas, A. D., Umeki, K., Gardini, D., Bates, R.B., Glarborg, P. (2016). Effects of several types of biomass fuels on the yield, nanostructure and reactivity of soot from fast pyrolysis at high temperatures. Applied Energy, 171, 468-482. doi: https://doi.org/10.1016/j.apenergy.2016.02.127
Publisher	Elsevier
Link to publisher's version	https://doi.org/10.1016/j.apenergy.2016.02.127
Item record	http://hdl.handle.net/10379/7357
DOI	http://dx.doi.org/10.1016/j.apenergy.2016.02.127

Effects of Several Types of Biomass Fuels on the Yield, Nanostructure and Reactivity of Soot from Fast Pyrolysis at High Temperatures

Anna Trubetskaya[a,*], Peter Arendt Jensen[a], Anker Degn Jensen[a], Angel David Garcia Llamas[b], Kentaro Umeki[b], Diego Gardini[c], Jens Kling[c], Richard B. Bates[d], Peter Glarborg[a,**]

[a] *Department of Chemical and Biochemical Engineering, Technical University of Denmark, Søltoft Plads, Building 229, Kgs. Lyngby 2800, Denmark*
[b] *Department of Engineering Sciences and Mathematics, Division Energy Science, Luleå University of Technology, 97187, Luleå, Sweden*
[c] *Center for Electron Nanoscopy, Technical University of Denmark, 2800 Kgs. Lyngby*
[d] *MIT, Department of Mechanical Engineering, 02139, Cambridge, MA, USA*

Abstract

This study presents the effect of biomass origin on the yield, nanostructure and reactivity of soot. Soot was produced from wood and herbaceous biomass pyrolysis at high heating rates and at temperatures of 1250 and 1400°C in a drop tube furnace. The structure of solid residues was characterized by electron microscopy techniques, X-ray diffraction and N_2 adsorption. The reactivity of soot was investigated by thermogravimetric analysis. Results showed that soot generated at 1400°C was more reactive than soot generated at 1250°C for all biomass types. Pinewood, beechwood and wheat straw soot demonstrated differences in alkali content, particle size and nanostructure. Potassium was incorporated in the soot matrix and significantly influenced

---

[*] Corresponding author. email: atru@kt.dtu.dk
[**] Corresponding author. email: pgl@kt.dtu.dk

soot reactivity. Pinewood soot particles produced at 1250°C had a broader particle size range (27.2 to 263 nm) compared to beechwood soot (33.2 to 102 nm) and wheat straw soot (11.5 to 165.3 nm), and contained mainly multi-core structures.

Keywords: fast pyrolysis, drop tube reactor, soot, potassium, reactivity

---

1. Introduction

Suspension firing of biomass is widely used for power generation and has been considered as an important step in reduction of greenhouse gas emissions. Biomass gasification offers high conversion efficiency and the possibility to handle different lignocellulosic materials to a wide variety of applications such as heat, electricity, chemicals and transport fuels [1]. Fast pyrolysis at high temperatures and at high heating rates is the initial step of the suspension biomass firing or biomass gasification depending on the reaction atmosphere. During pulverized biomass firing, particles first undergo rapid drying and devolatization, leading to the formation of char and volatiles. At temperatures below 1000°C, secondary reactions of volatiles produce mainly tars and small amounts of soot; at higher temperatures (1350-1400°C) these reactions produce soot and almost no tars [2, 3].

In order to reduce aerosol emissions and improvement of radiative heat transfer during combustion, it is necessary to understand how soot particle properties are correlated with fuel composition and operating conditions [4]. Understanding soot characteristics is also an important step for the optimization of gasification processes because the complete conversion of soot is desirable to increase syngas yields [5]. In suspension firing, soot can act as a

Nomenclature

β	Reflection broadening (2Θ)
κ	Heating rate (°C min^{-1})
λ	Wavelength (nm)
μ_g	Geometric mean of A_i
$\pi\ast$	π bonds
$\sigma\ast$	σ bonds
σ_g	Geometric standard deviation
Θ	Bragg angle (°)
A	Pre-exponential factor (s^{-1})
A_i	Set of numbers
A_{cr}	Area of TG crucible (mm)
$A_{G,\pi\ast}$	Relative area of π^* peak
$A_{G,\sigma\ast}$	Relative area of σ^* peak
d_p	Particle diameter (nm)
d_{002}	Interlayer distance (Å)
d_{sep}	Distance between graphene layers (nm)
E_a	Activation energy (kJ mol^{-1})
K_{Sc}	Scherrer constant
L_a	Lateral extension (Å)
L_c	Stacking height (Å)
m	Multiple cores
N	Number of layers
n	Number of experiments
R	Gas constant (J mol^{-1} K^{-1})
r	Ratio of relative areas
r_{diff}	Diffusion controlled rate (% min^{-1})
r_{max}	Maximal reaction rate (% min^{-1})
s	Single core
T	Heat treatment temperature (°C)
X	Conversion

radiating agent which promotes heat transfer in large flames [6]. Soot particles absorb heat and re-emit it as disperse radiation. Chen [7] reported that the production of both thermal and fuel NO_x in coal combustion depended on the reaction temperature, and thus, presence of the soot in a coal flame. Soot formation reduces NO_x levels by enhancing heat transfer [8]. Emissions of atmospheric aerosols, including soot, are associated with hazardous health effects, because they can contain polycyclic aromatic hydrocarbons (PAH), many of which are highly toxic and carcinogenic [9].

Studies of the physicochemical properties of soot derived from coal and hydrocarbon feedstocks [10–13] have identified a number of factors influencing reactivity: synthesis conditions, alkali content, particle size, and nanostructure [3, 5, 14–16]. Van Setten et al. [17] and Vander Wal et al. [11] point out that the feedstock of soot samples influence their properties and oxidation reactivity. Liati et al. [16] related the morphology of primary soot particles (size, shape and internal structure) to the factors which influence soot oxidation reactivity. Müller et al. [15] showed that larger graphene layer planes, larger crystallites, and concentrically orientated crystallites decrease soot reactivity. Some of the alkali metals contained in the biomass are vaporized and participate in soot formation and conversion reactions. Several studies have addressed the influence of alkali metals on the oxidation reactivity of soot from coal pyrolysis [18, 19]. Alkali is known to enhance oxidation of graphite [20] and suppress soot formation [21]. Small concentrations of alkali catalyze the reactions of carbonaceous materials with oxygen, carbon dioxide, hydrogen and water vapor [22, 23]. Neeft et al. [24, 25] investigated the effect of inorganic materials on graphite oxidation rate and soot accumulation in a diesel engine, and found that the intensity of contact between soot and alkali is a major predictor of soot oxidation rate. Potassium carbonates decompose at temperatures higher than 280°C, leading to increased reaction rates of graphite oxidation when alkali carbonates have good contact with the carbon[24]. Several studies [26, 27] reported that potassium bonded by oxygen to the carbonaceous matrix of soot increases the soot oxidation reactivity. Fredenhagen [28, 29] discovered alkali metal-graphite intercalates, and showed that graphite can react with alkali metals to form lamellar compounds in which the planar graphite arrangement remains largely preserved. Wen [18] suggested that potassium carbonates may catalyze the gasification of coal char and graphite to form carbon monoxides according to equations 1 and 2:

$$\mathrm{K_2CO_3 + 2C \rightarrow 2K + 3CO} \tag{1}$$

$$\mathrm{K + nC \leftrightarrow C_nK} \tag{2}$$

Potassium carbonate reacts with carbon to produce atomic potassium. Electron donor-acceptor (EDA) complexes are formed between potassium and the carbonaceous matrix of soot. Chen and Yang [20] suggested that alkali metals formed by reaction of K_2CO_3 with graphite might form C-O-K groups on the graphite surface and thereby enhance the reactivity of the carbon matrix.

Many soot reactivity studies are based on coal [13], liquid [10, 11] or gaseous hydrocarbons [12], but only a few have focused on biomass soot, which is formed by different chemical pathways [30]. Compared with soot from fossil fuel combustion, biomass soot particles are higher in inherent oxygen functionality as well as adsorbed organic species such as acids, alcohols and aldehydes [31]. Wiinikka et al. [32] concluded that the concentration of ash-forming elements significantly influences both the shape and nanostructure of pinewood soot particles during the entrained flow gasification of biomass. Septien et al. [3, 33] reported that initial fuel composition, particularly potassium content, influenced steam gasification rates of beechwood soot significantly. Overall, the conversion of biomass soot generated under combustion and gasification conditions remains poorly understood. In particular, the influence of biomass type (woody vs. herbaceous), reaction atmosphere (oxygen and carbon dioxide), and alkali metal impregnation/removal on the reactivity of soot prepared at high temperatures have not been previously examined. Little is unknown about the various biomass physicochemical properties that determine soot reactivity towards O_2 and CO_2.

In this study, therefore, the impacts of biomass origin, soot nanostructure, particle size and inorganic matter content on soot reactivity towards O_2 and CO_2 were investigated. The specific objectives of this study were to: (1) obtain knowledge about various stages in particle formation during suspension biomass combustion and high-temperature gasification (2) determine the reaction conditions which minimize soot formation to prevent clogging of downstream components and catalyst deactivation in high-temperature gasification (3) optimize soot-blower operation and heat transfer during pulverized biomass combustion.

2. Materials and methods

Pinewood, beechwood and Danish wheat straw were chosen for the fast pyrolysis study in a drop tube reactor (DTF). Fuel selection was based on the differences in the ash composition and plant cell compounds (cellulose, hemicellulose, lignin, extractives). The wood samples are low in ash, with slightly higher potassium and calcium contents in beechwood than in pinewood. Danish wheat straw is rich in silicon and alkali (K, Ca, Na).

Biomass soot samples collected during fast pyrolysis at 1250 and 1400°C were further investigated under O_2 and CO_2 gasification conditions in a thermogravimetric analyzer. Reactivities of wood and straw soot were compared using reaction rates calculated from the derived kinetic parameters. Ash analysis was carried out by X-ray fluorescence instrument only on the wheat straw soot to determine the composition of inorganic matter incorporated in the soot particle. Equilibrium calculations using the Factsage program and Fourier transform infrared spectroscopy (FTIR) analysis were performed to characterize water-soluble potassium compounds found in the wheat straw soot.

Reaction rates of non-treated beechwood and wheat straw soot were compared with leached samples to investigate the effect of potassium on soot reactivity. Soot samples were leached in deionized water by continuous stirring at room temperature for 30 minutes, followed by drying at 30°C in an oven desiccator. Graphite (Sigma-Aldrich, purity $> 99.99\,\%$, particle size $<$ $45\,\mu$m) reactivity was compared with soot reactivity in O_2 and CO_2 gasification. To study the catalytic effect of potassium, KNO_3 (Sigma-Aldrich, purity $> 99.999\,\%$) was diluted in deionized water and added to 50 mg graphite to obtain 20 wt. % or 30 wt. % potassium. Samples were dried at 30°C in an oven desiccator for 12 hours. Prior to gasification in 5 % volume fraction CO_2, graphite impregnated with 20 wt. % and 30 wt. % KNO_3 was kept at 500°C for 4 hours in N_2 using the thermogravimetric instrument to degas the basal plane of the graphite and to calcine the sample to release NO_2.

The generated soot samples were further characterized using X-ray diffraction (XRD) and electron energy-loss spectroscopy (EELS) to investigate the structural differences in organic (crystal, polycrystalline, and amorphous) and inorganic composition. The particle size and nanostructure of woody and herbaceous soot samples were analyzed by transmission electron microscopy (TEM).

2.1. Raw biomass characterization

The ultimate and proximate analysis of the woody and herbaceous biomass was carried out at TU Munich, Department of Energy Systems and shown in Table 1.

Table 1: Proximate, ultimate and ash analyses of fuels.

Fuel	Pinewood	Beechwood	Wheat straw
Proximate and ultimate analysis, (wt.% on dry basis)			
Moisture^a	5.1	4.5	5.5
Ash (550 °C)	0.3	1.4	4.1
Volatiles	86.6	79.4	77.5
HHV^b	21.6	20.2	18.8
LHV^b	20.2	19	17.5
^{a} wt.% (as received) ^{b} in MJ kg^{-1}			
C	53.1	50.7	46.6
H	6.5	5.9	6.1
N	0.06	0.13	0.6
S	<0.01	0.02	0.1
Cl	0.01	0.02	0.1
Ash compositional analysis, (mg kg^{-1} on dry basis)			
Al	10	10	150
Ca	600	2000	2500
Fe	20	10	200
K	200	3600	11000
Mg	100	600	750
Na	30	100	150
P	6	150	550
Si	50	200	8500
Ti	2	<8	10

2.2. Fast pyrolysis in drop tube furnace

Soot matter was obtained from fast pyrolysis experiments in the drop tube reactor (DTF) at 1250 and 1400°C. The DTF setup was described in detail by Goktepe et al. [34]. The experiments were conducted by feeding ≈ 5 g of biomass at a rate of 0.2 g min^{-1}. Both primary (0.18 m^3 min^{-1} measured at 20°C and 101.3 kPa) and secondary (0.0048 m^3 min^{-1} measured at

20°C and 101.3 kPa) feed gases were N_2. The residence time of fuel particles was estimated to be about 1 s, taking into account density changes during pyrolysis [35].

Biomass was rapidly heated and reacted while it fell down through the reactor. Reaction products were separated into coarse particles (mainly char and fly ashes), fine particles (mainly soot and ash aerosols), and permanent gases. Soot particles passing the cyclone (cut size 2.5μm) were captured from the product gas flow by a grade QM-A quartz filter with a diameter of 50 mm (Whatman, GE Healthcare Life Science).

2.3. Soot analysis

Elemental analysis. The elemental analysis was performed on two instruments of the same model (Eurovector, model EA3000). Acetanilide was used as a reference standard. The ash content was determined using a standard ash test at 550°C, according to the procedure described in DIN EN 14775.

Ash compositional analysis. The ash compositional analysis was performed by an X-ray fluorescence instrument (Shimadzu, model EDX 800-HS) at TU Munich. Prior to the XRF analysis, soot samples were pre-heated in oxygen at 5°C min^{-1} up to 550°C and kept at that temperature for 7 h. The generated ash (about 200 mg) was initially mixed and then pressed with a special wax (mixture ratio 1:5). The Cl and S content in the ash was analyzed by ICP-OES/IC at TU Wien. The ash sample was dissolved in ultrapure water at 120°C for 1 h, and then the solution was filtered and analyzed by ICP-OES/IC.

FTIR Spectroscopy. The wheat straw soot samples were analyzed by a Thermo Nicolet 6700 FTIR spectrometer equipped with a Golden gate (diamond) ATR accessory and DTGS (KBr) detector. All transmission spectra were obtained in the 4000-600 cm^{-1} range by 100 scans at 4 cm^{-1} resolution. For background, 200 scans were acquired. A good contact between sample and ATR-crystal surface was ensured by the pressure device of the unit (up to 30000 psi) [36]. All samples were measured in triplicate.

X-ray diffraction. The crystalline constituents of the soot matter were characterized using a Bruker D8 AXS X-ray diffractometer with (Cu-Kα1, λ = 1.54056 Å and Cu-Kα2 radiation, λ = 1.54439 Å) operating in Bragg-Brentano (reflection) mode, using a secondary graphite monochromator, and a scintillation detector, in the range 5 to 80 degrees for 12.5 hours. The sample was placed in a small cup rotated during data collection. The interlayer distance d_{002}, based on similarities with the graphite structure, is calculated by Bragg's equation [37]:

$$d_{002} = \frac{\lambda}{2sin\theta_{(002)}} \tag{3}$$

θ is a Bragg angle. The stacking height (L_c) of the crystallites was estimated using the Scherrer's formula with the constant K_{Sc} = 0.9 [38]:

$$L_c = \frac{0.9 \cdot \lambda}{\beta(2\theta)_{(002)} \cdot cos\theta_{(002)}} \tag{4}$$

B(2θ) is the sample broadening of the reflection, calculated in radians, at full width half maximum (FWHM). The lateral extension (L_a) was calculated using the Scherrer equation with the constant K_{Sc} = 1.84 for the two-dimensional lattice reflections of the type (hk0) [38]:

$$L_a = \frac{1.84 \cdot \lambda}{B(2\theta) \cdot cos\theta} \tag{5}$$

The number of layers (N) is determined using L_c in equation 6 with the assumption that a carbon material consists of parallel layers [39]:

$$N = \frac{L_c + d_{002}}{d_{002}} \tag{6}$$

The collected XRD pattern were analyzed using Crystallographica Search-Match software (Version 3,1,0,0). The instrumental reflection broadening was subtracted from the experimental pattern by Winprep software.

Thermogravimetric analysis. The reactivity of soot in 5 % volume fraction O_2 or CO_2 ($50\,cm^3\ min^{-1}$ of O_2 or CO_2 and $95\,cm^3\ min^{-1}$ of N_2 measured at 20°C and 101.3 kPa) was determined using a thermogravimetric instrument (Netzsch, STA 449 F1) by loading 3 mg of sample in an Al_2O_3 crucible and heating from 35 to 1350°C in O_2 and from 35 to 1450°C in CO_2 at a constant heating rate of 10°C min^{-1}. The initial sample mass and heating rate used in the TG experiments were selected to minimize possible mass transfer limitations that may occur by O_2 / CO_2 gasification concentration gradients through the TG crucible down to the particle bed, through the particle bed, and inside of soot particle agglomerates [40, 41]. The results of Abian et al. [42] showed that less than 3.5 mg of soot samples should be applied to avoid mass transfer limitations using a heating rate of 10°C min^{-1} in 10 % volume fraction CO_2 gasification. The kinetic parameters of soot samples were derived by the integral method presented by Coats and Redfern [43]. Through integral transformation and mathematical approximation, the linear equation was expressed in the form:

$$ln\left(-\frac{ln(1-X)}{T^2}\right) = ln\left(\frac{A \cdot R}{\kappa \cdot E_a}\right) - \frac{E_a}{R \cdot T} \tag{7}$$

In equation 7, κ is the heating rate and R is the gas constant. A plot of ln(-ln(1-X) T^{-2}) versus T^{-1} gives a straight line whose slope and intercept determine the values of the activation energy (E_a) and pre-exponential factor (A). The results of Qin et al. [5] showed that a first order reaction model in both soot mass and gasification agent can describe the experimental results well.

The reactivities of wood and wheat straw soot samples were compared using reaction rates calculated from the derived kinetic parameters (A and E_a) at a fixed oxidation / gasification temperature of 600°C and 1100°C.

N_2 adsorption analysis. The specific surface area (SSA) of biomass chars was determined based on nitrogen adsorption at the boiling point (77 K). To remove surface contaminants, the samples were heated to 350°C in a dry N_2 flow prior to the measurement. The multipoint Brunauer-Emmett-Teller (BET) theory with seven points in the range of p/p_0 from 0.01 to 0.2 is applied on the BET instrument (Quantachrome iO2). BET equation was used to determine the specific surface area [44].

Soot pretreatment for the microscopy. Prior to the microscopy, soot samples were kept at 350°C for 4 hours in a thermogravimetric instrument to reduce the amount of volatiles. However, the thermogravimetric curves (supplementary Figure S-9) quantified the remaining volatiles yield to be less than 5 %. Samples were grounded in a mortar to ensure a homogeneous particle distribution and dry dispersed on a lacey carbon copper grid.

Transmission electron microscopy. Soot morphology and composition were studied using either a FEI Titan transmission electron microscope operated at 120 keV or a FEI Tecnai operated at 200 keV, both equipped with an Oxford Instruments X-Max SDD EDS detector.

Electron energy-loss spectroscopy (TEM-EELS). EELS analysis of soot samples was performed in the FEI Titan presented before, equipped with a Gatan GIF Tridiem spectrometer. For anisotropic materials like graphite and soot, the fine structure of the ionization edges is dependent on the orientation of the sample and the collection angle of the spectrometer. To compare different samples, the so called magic-angle condition is used, which minimizes the influence of the anisotropic structure [45–49]. Magic-angle conditions were chosen by acquiring a spectrum of the C-K edge (about 285 eV) in parallel illumination under two different tilt angles of the sample. The right parameters are found as both spectra matches in shape and relative intensity. The EELS spectra are background subtracted and corrected for multiple scattering.

Particle size distribution analysis using TEM. The particle size of soot samples was estimated manually from TEM images using the ImageJ software. The clearly visible primary particles were selected for accurate analysis. The data were assessed to establish particle size distributions. For the size analysis, soot particles were assumed spherical. Particle size analysis was conducted on 50 particles at each operating condition. The geometric standard deviation was calculated as shown in equation 8 [50]:

$$\sigma_g = exp\left(\sqrt{\frac{\sum_{i=1}^{n} ln\left(\frac{A_i}{\mu_g}\right)^2}{n}}\right) \tag{8}$$

μ_g is the geometric mean of a set of numbers A_i. The standard deviation was calculated for curvature, fiber length (see definition below) and separation distance of graphene layers.

Graphitic structure. The term graphitic structure was used to compare soot nanostructure with graphitic carbon in terms of graphene layer length, curvature and parallelism within the primary soot particles. The amorphous core of the soot particles refers to the short-ranged structures. The curvature of a single graphene sheet is defined in equation 9:

$$Curvature = \frac{Length}{Fiber\ \ length} \tag{9}$$

The length is a straight line that connects both ends of a graphene sheet. The fiber length is a contour or arc length (supplementary Figure S-12). Both length and fiber length were estimated by Gatan Digital Micrograph software according to method of Müller et al. [14]. The part of the image with the more visible graphene layers was magnified to a size of 10 nm x 10 nm, and both length and fiber length were manually determined by the software ruler which draws a straight or contour line to connect both ends of a graphene sheet.

3. Results

3.1. Reactivity

Figure 1 shows differential weight loss curves (DTG) for the 5 % volume fraction O_2 and 5 % volume fraction CO_2 gasification of soot samples. The DTG curves show a single broad peak in both O_2 oxidation and CO_2 gasification, indicating a heterogeneous soot mixture with respect to the composition and particle size as suggested by Russell et al. [51].

The oxidation of beechwood and wheat straw soot at both preparation temperatures took place at nearly the same temperature range from 350 to 550°C, whereas the maximum reaction rate of pinewood soot was shifted to temperatures about 100°C higher than for the other biomasses (in O_2 between 450 and 700°C). The pinewood soot was clearly less reactive in comparison to beechwood and wheat straw soot. The pinewood soot reactivities at 1250 and 1400°C in the CO_2 atmosphere were nearly similar to graphite with the peak temperature at 1350°C.

The relative importance of external diffusion on the overall soot oxidation / gasification in the TG experiments was evaluated by comparing of the observed maximal reaction rate (r_{max}, % min^{-1}) with the calculated diffusion rate (r_{diff}, % min^{-1}) of O_2/CO_2. The influence of convective flow on the mass transfer inside the crucible was assumed to be negligible, and so mass transport occurs by molecular diffusion only.

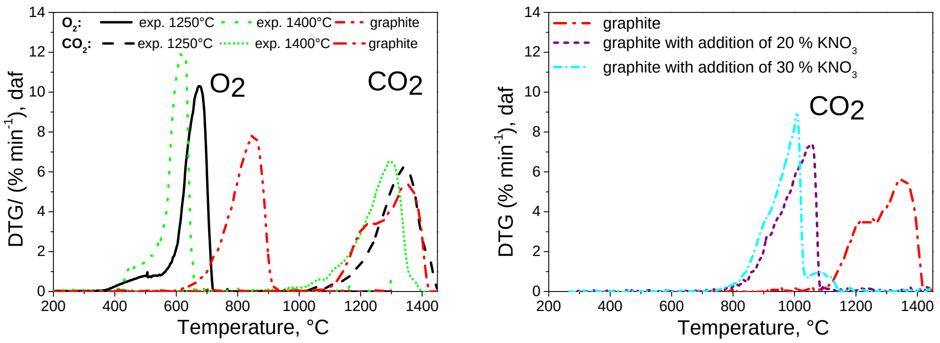

1(a): Pinewood soot in O_2 and CO_2 1(b): Graphite with added KNO_3 in CO_2

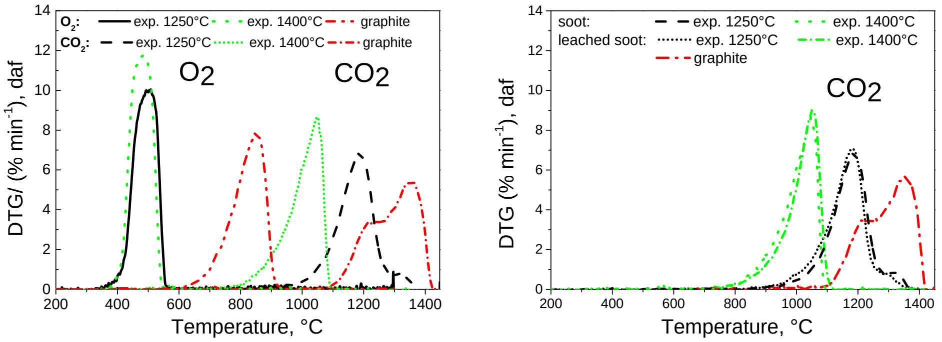

1(c): Beechwood soot in O_2 and CO_2 1(d): Leached beechwood soot in CO_2

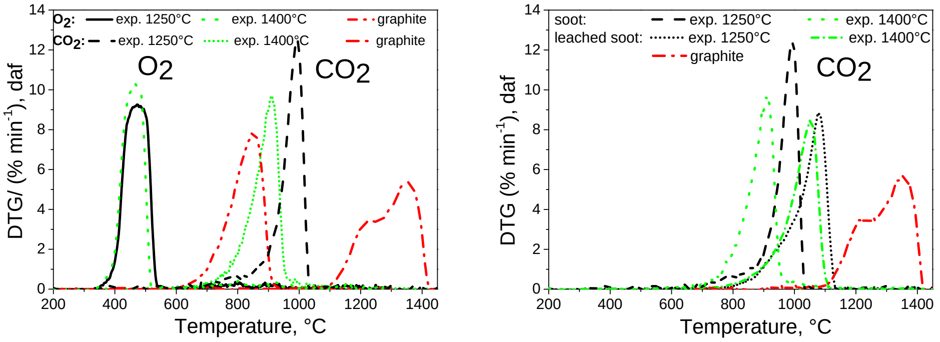

1(e): Wheat straw soot in O_2 and CO_2 1(f): Leached straw soot in CO_2

Figure 1: (a),(c),(e) DTG curves of pinewood, beechwood, wheat straw soot samples and graphite in (5 % volume fraction O_2 + 95 % volume fraction N_2)(straight line) and (5 % volume fraction CO_2 + 95 % volume fraction N_2) (dashed line) (b),(d),(f) 20 wt. % KNO_3 and 30 wt. % KNO_3 added to graphite, wheat straw and beechwood soot samples prepared at 1250 and 1400°C and leached in deionized water. The reactivity measurements of leached soot samples were carried out in (5 % volume fraction CO_2 + 95 % volume fraction N_2). The DTG curves of soot are black (1250°C), green (1400°C) and of graphite (red).

Soot samples were assumed to be non-porous. The mass transfer of product gases on the reaction was neglected, and the temperature within the soot layer was assumed uniform. Furthermore, it was assumed that the soot particles were distributed equally in the TG crucible.

Table 2: Kinetic parameters for O_2 and CO_2 reactivity of pinewood, beechwood, wheat straw, leached wheat straw, leached beechwood soot samples, pyrolyzed at 1250 and 1400°C in the drop tube reactor, and graphite and impregnated graphite with 20 wt. % and 30 wt. % KNO_3.

Temperature	E_a	A	r_{max} at 600°C	E_a	A	r_{max} at 1100°C
°C	kJ mol^{-1}	s^{-1}	s^{-1}	kJ mol^{-1}	s^{-1}	s^{-1}
		O_2			CO_2	
			Pinewood soot			
1250	250	$4\cdot10^{11}$	$4.5\cdot10^{-4}$	270	$1\cdot10^{6}$	$7\cdot10^{-5}$
1400	252	$6\cdot10^{11}$	$4.9\cdot10^{-4}$	275	$6\cdot10^{6}$	$2\cdot10^{-4}$
			Beechwood soot			
1250	155	$1\cdot10^{8}$	$7\cdot10^{-2}$	235	$5\cdot10^{5}$	$6\cdot10^{-4}$
1400	154	$1\cdot10^{8}$	$7\cdot10^{-2}$	195	$2\cdot10^{5}$	$7\cdot10^{-3}$
			Wheat straw soot			
1250	145	$5\cdot10^{7}$	0.1	183	$1\cdot10^{5}$	0.01
1400	147	$1\cdot10^{8}$	0.15	187	$5.6\cdot10^{5}$	0.04
			Leached beechwood soot			
1250				239	$2.3\cdot10^{5}$	$8\cdot10^{-4}$
1400				199	$2.3\cdot10^{5}$	$6\cdot10^{-3}$
			Leached wheat straw soot			
1250				208	$3\cdot10^{5}$	$4\cdot10^{-3}$
1400				194	$1\cdot10^{5}$	$5\cdot10^{-3}$
			Graphite			
pure	195	$5\cdot10^{6}$	$4\cdot10^{-9}$	276	$3\cdot10^{6}$	$1\cdot10^{-6}$
20 % KNO_3				236	$1\cdot10^{7}$	0.01
30 % KNO_3				240	$4\cdot10^{7}$	0.02

The maximal reaction rate (r_{max}) measured by the thermogravimetric instrument is shown as the first derivative (DTG) at the maximal temperature in Figure 1. The mass transfer (r_{diff}) of O_2/CO_2 transfer to the surface of the soot particle bed was estimated (supplementary Table S-6). The calculated r_{max}/r_{diff} ratio in the supplemental material showed that the oxidation / gasification reaction in the TG analysis was mainly influenced by chemical kinetic limitations, and to a minor extent controlled by the external diffusion.

It is interesting to observe that for both O_2 and CO_2, the maximal reaction rate was shifted to lower temperatures with increasing soot formation temperature, confirming previous results of Qin et al. [5] and Septien et al. [33], and contrary to the usual observation that the reactivity of carbonaceous materials decreases with increasing heat treatment temperature [5]. The reason for the increased reactivity observed in the TG experiments with increasing heat treatment temperature in the drop tube reactor will be discussed below.

The differences in the alkali content and nanostructure of woody and herbaceous soot samples are expected to influence the soot reactivity [16, 20, 21, 32, 52, 53]. The impact of alkali metals on the soot reactivity appears to be related to the differences in potassium content among woody and herbaceous biomass. The elemental potassium, bonded to the soot matrix in phenolate groups or intercalated in graphene layers, determines the catalytic gasification rate [19, 54]. Chen and Yang [20] suggested that the alkali metal formed by reaction of K_2CO_3 with graphite might form C-O-K groups on the surface and thereby enhance the reactivity of the carbon substrate. In the present study, the catalytic effect of potassium on the soot reactivity was investigated by impregnating graphite with KNO_3. Graphite with added 20 wt. % and 30 wt. % KNO_3 was subjected to pretreatment in the TG analysis in N_2 for 4 hours to promote the dispersion of potassium throughout the graphite [18, 55] and later to gasification in 5 % volume fraction CO_2. Figure 1(b) shows a shift of the maximal reaction rate to lower temperatures from 1350°C to 1050°C and 980°C. This shows that the potassium impregnation increased the reactivity of a graphite powder during CO_2 gasification.

The catalytic effect of alkali on soot reactivity was also investigated by removal of water-soluble potassium compounds from wheat straw and beechwood soot. The inorganic matter content of the wheat straw soot prepared at 1250 and 1400°C after leaching decreased from 12 to 4 % and from 21 to 7 % according to thermogravimetric experiments in 5 % volume fraction O_2. The ash content of beechwood soot after leaching remained unchanged. Figure 1(d) shows that the maximal reaction rate of leached wheat straw soot prepared at 1250 and 1400°C shifted to higher temperatures, from 980 to 1070°C and from 900 to 1050°C, showing that the removal of potassium leads to a lower reactivity of the soot. The estimated activation energies of wheat straw soot prepared at these temperatures increased from 183 to 208 kJ mol^{-1} after leaching and from 187 to 194 kJ mol^{-1} in Table 2. In contrast, the changes in activation energy of beechwood soot were small. Leaching of the beechwood did not alter its reactivity as shown by the identical peak temperatures for each soot sample preparation temperature (980°C for soot prepared at 1400°C and 1050°C for soot prepared at 1250°C). Potassium remaining in wheat straw soot and beechwood after the leaching was probably bonded to the soot matrix in oxygen-containing surface groups (i.e. carboxylic acids, phenolate) or by the intercalation in graphene layers [56, 57]. This led to a higher reactivity of leached soot in CO_2 gasification compared to the potassium lean pinewood soot where the activation energies remained higher ($\approx 275\,\mathrm{kJ\ mol^{-1}}$). These results strongly suggest that potassium has a dominating influence on the soot reactivity.

3.2. X-ray diffraction of soot

As seen in Figure 2, the XRD analysis of soot indicated formation of turbostratic patterns correlated to the graphite structure. The broad reflections at 25° and 43.6° show the development of a crystalline phase, where if axis "c" is perpendicular to and axes "a" and "b" lie on the plane layer, the crystalline reflection will be of type 001 and the two-dimensional reflection will be of the index type "hk0". The reflection at 25° was assigned to the parallel graphene layers, which are spaced at a well-defined inter-planar distance d_{002}, corresponding to 002 reflection of graphite. The polyaromatic structures might be aligned in a similar manner as graphene layers. The reflection at 43.6° represented two-dimensional reflections, which arise from the ordering of carbon atoms inside the graphite layers, which take independently all reflections in space [37]. A broadening of both reflections was attributed to the effect of the small crystalline size as quantified in Table 3 [58].

The average extension of graphene layers (L_a) and their thickness (L_c) were calculated for soot, prepared at 1250 and 1400°C, and shown in Table 3. The L_c and L_a values indicated no significant influence of temperature and biomass origin on the soot carbon structure. The average extension of graphene stacks (L_a) in the biomass soot was quantitatively similar to that of low-rank coal char (37.6 Å of naphthalene origin) with 4-10 graphene layers (N) [59, 60] and different from the graphite structure (L_a > 100 Å) [61]. The interlayer distance (d_{002}) was calculated for all soot samples (3.56 Å) by equation 3, which was higher than that of graphite (3.34 Å) [37]. However, the interlayer distance was comparable with the value typically found for carbon black interlayer distance (3.4-3.6 Å) [62, 63]. The lateral height (or grain size) was comparable for all six measured samples.

Table 3: Crystallite dimensions ($L_{c,002}$, $L_{a,100}$), determined from XRD measurements.

	$L_{c,002}$, Å		**$L_{a,100}$, Å**		**N layers**	
Soot	**1250°C**	**1400°C**	**1250°C**	**1400°C**	**1250°C**	**1400°C**
Pinewood	18.5	19.8	37.5	37.6	6	7
Beechwood	18	19.2	33	34	6	6
Wheat straw	13.3	13.4	33	36	5	5

The present results show that soot from woody and herbaceous fuels could be described as distorted graphite structures with a low graphitic stacking of parallel graphene layers, probably embedded in amorphous carbon. The XRD analysis did not show any significant differences between woody and herbaceous soot samples in terms of graphitization. The additional reflections, detected by the XRD measurements of wheat straw soot, represented the inorganic matter such as KCl.

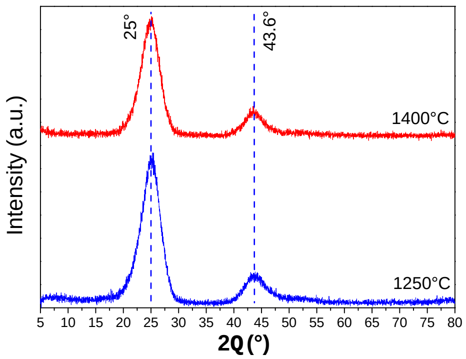

2(a): Pinewood soot

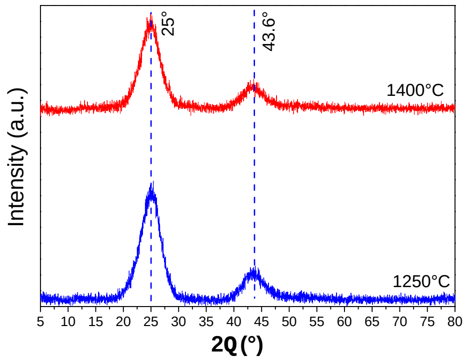

2(b): Beechwood soot

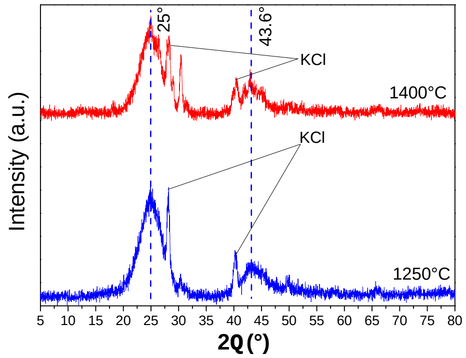

2(c): Wheat straw soot

Figure 2: XRD analysis of pinewood, beechwood and wheat straw soot samples (1250 and 1400°C) in the drop tube reactor.

3.3. Soot yield and inorganic matter effect

Figure 3 illustrates that the soot yields from pinewood pyrolysis at 1250 and 1400°C were the highest (8.3 % and 6.9 wt. % daf), whereas the wheat straw soot yields were the lowest (2.7 and 3.3 wt. % daf). Trubetskaya et al. [64] showed that the higher concentration of lignin and resin acids in woody samples may lead to a larger formation of PAH precursors and thus higher soot yields.

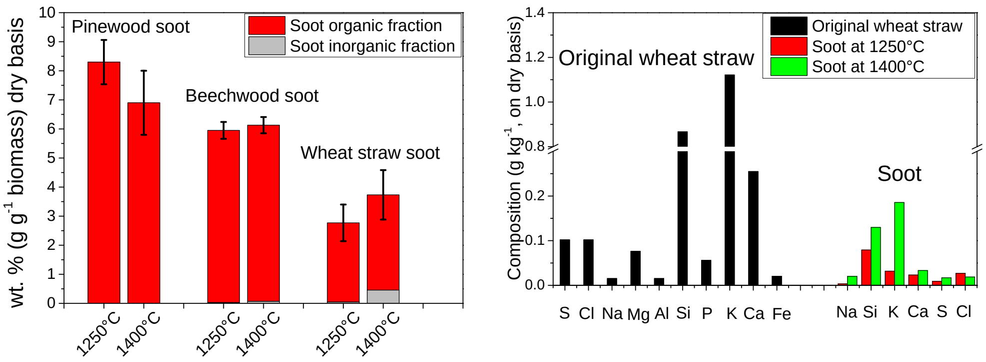

3(a): Organic and inorganic fractions

3(b): Ash analysis of original wheat straw and its soot (1250 and 1400°C)

Figure 3: (a) The total yield of soot is separated in inorganic and organic fractions of pinewood, beechwood and wheat straw (1250 and 1400°C) shown in wt. % relative to the original biomass (g g^{-1} on dry basis); (b) Ash compositional analysis of wheat straw soot (1250 and 1400°C) which is shown in g kg^{-1} on dry basis.

The soot matter from pinewood, beechwood and wheat straw consists of organic and inorganic fractions (supplementary Tables S-2 and S-3). The inorganic content of soot was determined by thermogravimetric analysis in 5 % volume fraction O_2. The ash composition analysis of wheat straw soot and original biomass was performed by an X-ray fluorescence instrument. The wheat straw soot showed an increasing inorganic fraction when the heat treatment temperature increased from 1250 to 1400°C, whereas the inorganic matter of the wood soot samples remained small at a level of 0.03 wt. %. Knudsen et al. [65] experimentally showed that at high temperatures, KCl sublimation and potassium silicates reactions are dominant during devolatilization, depending on the availability of Si, Cl, Ca and Mg in the original fuel. The lower Cl content in the wood might indicate that potassium was released in the form of KOH or to a minor extent in the form of KCl [66]. The high Cl content in the original wheat straw enhances the release of potassium, leading to the higher release of inorganic matter with the increasing temperature [67].

The ash compositional analysis was carried out only on the wheat straw soot, due to the high availability of this sample. The ash analysis indicated significant levels of K, Cl, S and Si, which in addition was supported by the transmission electron microscopy results. As seen in Figure 3(b), a low content of sulfur (up to about 0.02 wt. %) was observed in both straw soot samples. Thermodynamic equilibrium calculations using the Factsage program, with input parameters as listed in supplementary Table S-1, show that sulfur was most likely released as H_2S during biomass pyrolysis, in agreement with experimental results from Puri et al. [68, 69]. Possibly the hydrogen sulfide reacts with the soot active sites or by reaction with metals, as observed experimentally by Cal et al. [70]:

$$\mathrm{C} + \mathrm{H_2S} \rightarrow \mathrm{C\text{-}S} + \mathrm{H_2} \tag{10}$$

$$\mathrm{C\text{-}M} + \mathrm{H_2S} \rightarrow \mathrm{C\text{-}M\text{-}S} + \mathrm{H_2} \tag{11}$$

The water-soluble alkali found in wheat straw soot can be related to the formation of KCl, KOH, $KHCO_3$ and K_2CO_3 salts. Equilibrium calculations and X-ray diffraction reflections in this study suggest an incorporation of water-soluble KCl in the wheat straw soot. Figure 3(b) shows that the soot matter prepared at 1400°C contained a higher K fraction than soot prepared 1250°C. However, the K fraction which reacted / deposited with the wheat straw soot at 1400°C was significantly larger than the fractions of S and Cl.

Figure 4 shows the IR spectra of wheat straw soot, and the assigned species to each IR band.

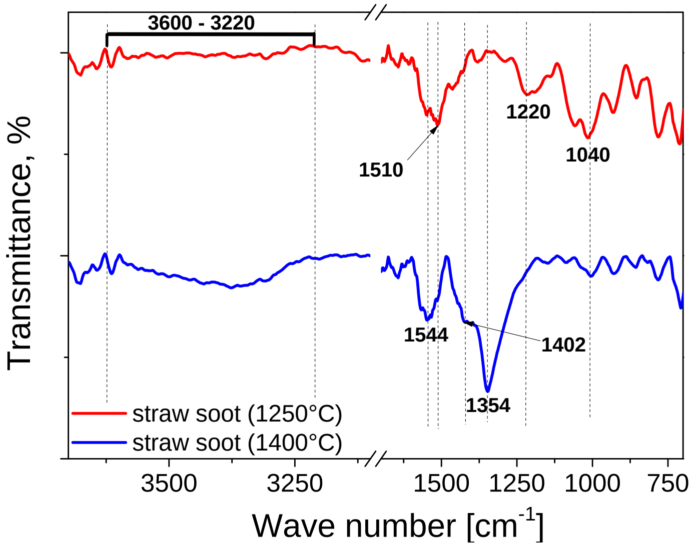

Figure 4: Experimental IR spectra of wheat straw soot prepared (1250 and 1400°C). The IR spectra was assigned to: 3600-3200 cm^{-1} - hydroxyl group [71, 72], 1550-1500 cm^{-1} - chelating bidentate carbonate [73], 1402 cm^{-1} - ionic carbonate [73], 1354 cm^{-1} - chelating bidentate carbonate [73], 1220 cm^{-1} - bicarbonate [74] and 1040 cm^{-1} - organic carbonate bond to K^+ [75, 76].

The IR measurements indicated that potassium was mostly deposited on the wheat straw soot surface as potassium carbonate and potassium bicarbonate. Due to the high content of potassium in wheat straw soot, the band at 1220 cm^{-1} was related to formation of potassium bicarbonate. The band completely disappears at the higher heat treatment temperature of soot. The 1354, 1402 and 1550-1500 cm^{-1} bands [73] were found in both wheat soot samples prepared at 1250 and 1400°C, and were associated with the formation of potassium carbonate. Chen and Yang [20] suggested that potassium can be anchored in the phenolate (C-O-K) groups to the carbon surface of soot samples. Potassium could also evaporate from wheat straw as potassium hydroxide, deposit on soot surface and react with the carbonaceous material according to equation 12:

$$\mathrm{KOH} + \text{soot-OH} \leftrightarrow \text{soot-OK} + \mathrm{H_2O} \tag{12}$$

Mul et al. [21] ascribed the 1118 cm^{-1} and 1300 cm^{-1} bands to the potassium phenolate. In the present study, the 1040 cm^{-1} band may be associated with the vibrations of complex organic-like carbonate species bonded to the K^+ ion (C-O-K) [75, 76]. Moreover, the measured IR signal is proportional to the number of groups in the path of IR light. In the present study, the concentration of potassium bonded to the soot matrix in the oxygen-containing surface groups was probably low, leading to the low IR signal. Ibrahim et al. [77] attributed the 1532 cm^{-1} and 1348 cm^{-1} bands to the asymmetric and symmetric stretching of carboxyl group bonded to the K^+ ion. However, these bands were not detected in the present study, probably indicating a low content of carboxyl surface groups bonded to potassium in the wheat straw soot.

Wen [18] suggested the formation of the potassium-carbon complexes or intercalates (lamellar compounds). Soot samples with a structure closer to graphite could more easily intercalate potassium due to the high electronegativity of graphite [78]. The oxygen lean beechwood soot with the more graphitic structure compared to pinewood soot may intercalate potassium similarly to graphite as discussed in later sections.

3.4. Particle size analysis

TEM investigations were carried out to examine the primary particle size characteristics of the soot samples prepared at 1250 and 1400°C. The size distribution of the primary soot particles was plotted as a fraction of the number of particles in each size range as shown in Figure 5. The calculated geometric mean diameters varied from 30.8 nm up to 77.7 nm, and were similar to the values reported for biomass smoke (30-50 nm) in other studies [79, 80]. The primary particle size range gives an interesting insight to the soot formation process, which seems to be influenced by the operating conditions and biomass origin. Ross et al. [81] hypothesized that the amount of volatiles, which is high for woody biomass, is a major factor influencing the soot yield and particle size. It was observed that the mean diameter of soot samples prepared at 1250°C was larger, while the particle size distribution was less uniform compared to soot samples prepared at 1400°C. Higher heat treatment temperatures led to a narrower particle size distribution for both the woody and herbaceous biomass soot.

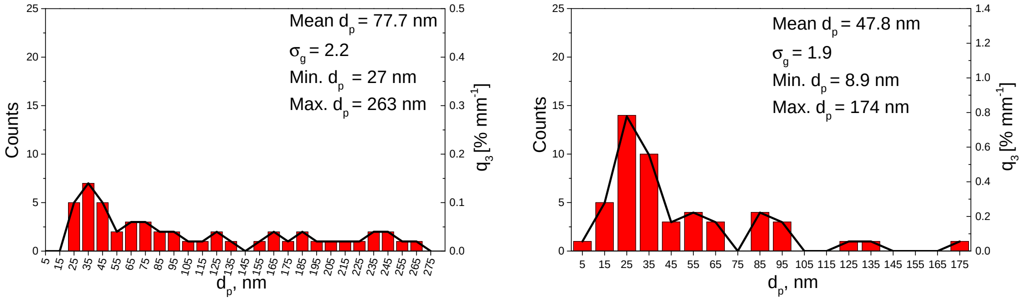

5(a): Pinewood soot (1250°C)

5(b): Pinewood soot (1400°C)

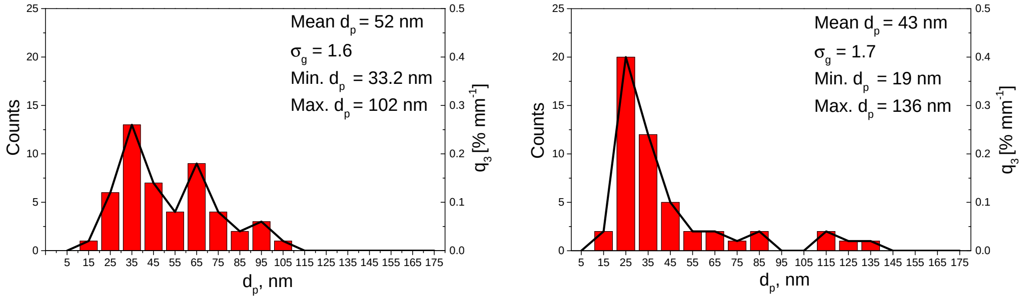

5(c): Beechwood soot (1250°C)

5(d): Beechwood soot (1400°C)

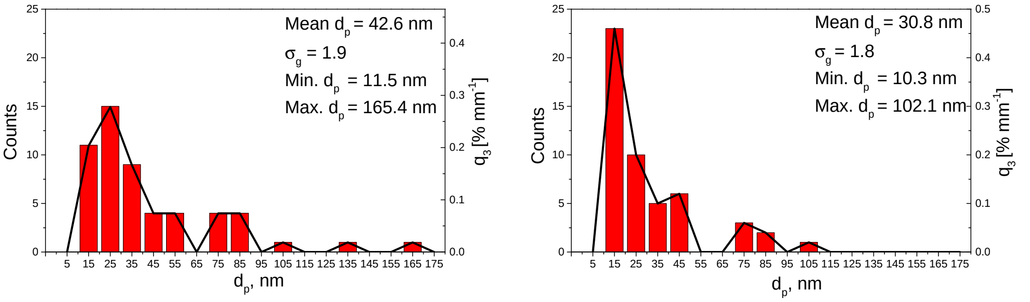

5(e): Wheat straw soot (1250°C)

5(f): Wheat straw soot (1400°C)

Figure 5: Particle size distributions of pinewood, beechwood and wheat straw soot samples (1250 and 1400°C). The particle size analysis was performed by the TEM. The mean diameter with the standard deviation, minimal and maximal diameters are illustrated. On the left y-axis, the number of particles in the fraction is shown , whereas on the right y-axis, the particle frequency distribution, based on volume (q_3) is illustrated in % mm^{-1}. The analysis was performed on 50 particles in each sample.

Specifically, the mean diameter of pinewood soot particles prepared at 1250°C was almost twice as large as that of soot prepared at 1400°C. The pinewood soot produced at 1250°C resulted in the broadest particle size distribution from 27 to 263 nm compared to beechwood soot from 33.2 to 102 nm and wheat straw soot from 11.5 to 165.4 nm. The high potassium content in wheat straw may have inhibited coagulation of soot particles, leading to the smaller particle size of 30.8 nm compared to other soot samples. The larger mean diameter of pinewood soot particles was also confirmed by the specific surface area measurements using N_2 adsorption as shown in Table 4.

Table 4: BET surface area (SSA) of pinewood, beechwood and wheat straw soot samples, determined by N_2 adsorption $m^2\ g^{-1}$.

Soot	**1250°C**	**1400°C**
	$m^2\ g^{-1}$	
Pinewood	37.9	38.4
Beechwood	56.3	74.3
Wheat straw	70	92.3

The beechwood and wheat straw soot particles attained a larger surface area (56.3-92.3 $m^2\ g^{-1}$) than the pinewood soot (37.9-38.4 $m^2\ g^{-1}$). The surface areas of pinewood soot particles generated at 1250°C and 1400°C were similar, while the mean particle size determined by TEM microscopy decreased from 77.7 to 47.8 nm. The surface area determined by N_2 adsorption might not only reflect the surface area of individual particles, but also be influenced by the type of agglomerate. TEM characterization gives information about individual particles.

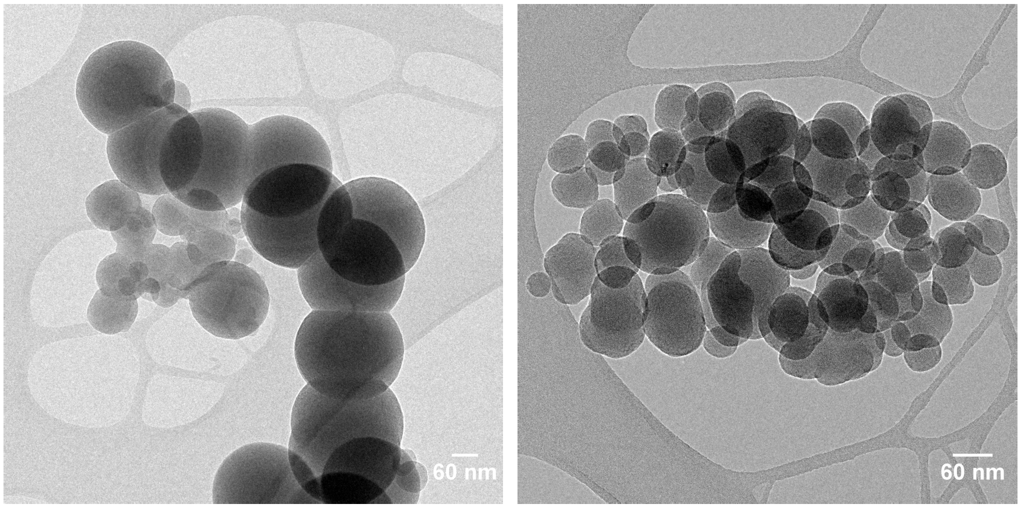

6(a): Pinewood tar balls (1250°C) 6(b): Non-spherical pinewood soot (1250°C)

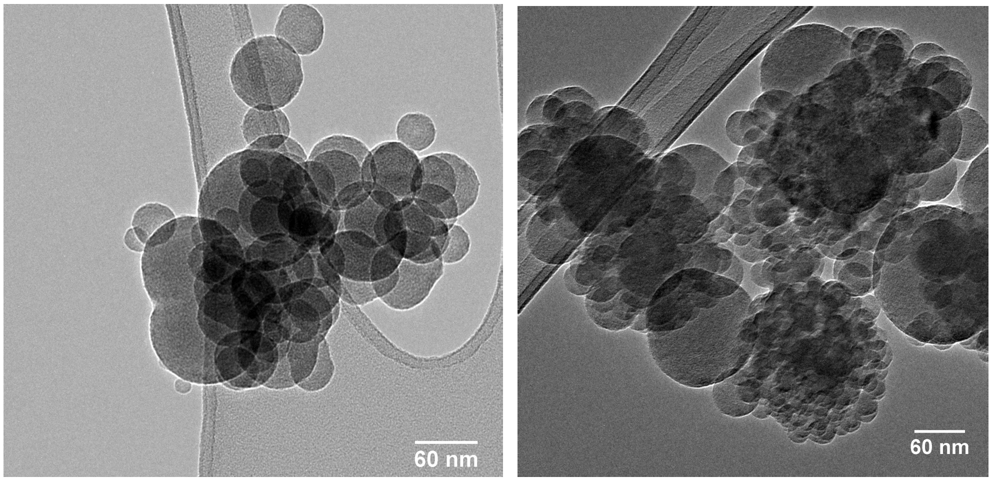

6(c): Beechwood soot (1400°C) 6(d): Wheat straw soot (1400°C)

Figure 6: TEM images of particle agglomerates of pinewood, beechwood and wheat straw soot samples (1250 and 1400°C). (a) Pinewood tar balls (1250°C) (b) Non-spherical pinewood soot (1250°C) (c) Beechwood soot (1400°C) (d) Wheat straw (1400°C)

The larger particles with a diameter from 100 to 263 nm appear to be tar balls as reported by Posfai et al. [82, 83]. Pinewood produced at 1250°C formed chain-like structures of tar balls, whereas wheat straw soot particulate formed large agglomerates consisting of smaller particles dispersed on the tar ball surface as shown in Figure 6. Posfai et al. [82, 83] suggested the formation of tar balls from low volatile organic compounds, such as lignin pyrolysis products under smoldering conditions. Wiinikka et al. [32] observed similar larger soot particles (100-300 nm) at high temperatures in pinewood pressurized gasification. Arora et al. [84] reported that under smoldering conditions, the nature of lignocellulosic materials (wood, cow dung, mustard stalks) influenced the formation of tar balls, leading to various particle size distributions. The formation of larger particles at 1250°C may be related to a higher concentration of PAH components, which contribute to the growth of the soot particles. At higher temperatures, cracking of the PAH components would be promoted, limiting their contribution to the growth.

3.5. Surface structure

The nanostructure of the soot, prepared at 1250 and 1400°C, was studied by TEM as shown in Figure 7. The woody and herbaceous soot appeared as agglomerates. The nanostructure of the soot particles was well-ordered. The primary soot particles exhibited a core-shell structure, with both single and multiple cores as shown in Figure 7.

The primary particles in pinewood soot produced at 1250°C consisted of a mixture of single and multi-core structures, but at higher temperatures they contained mainly single cores, similar to the wheat straw soot prepared at 1250 and 1400°C. The primary particles in beechwood soot also possessed a mixture of single and multiple cores.

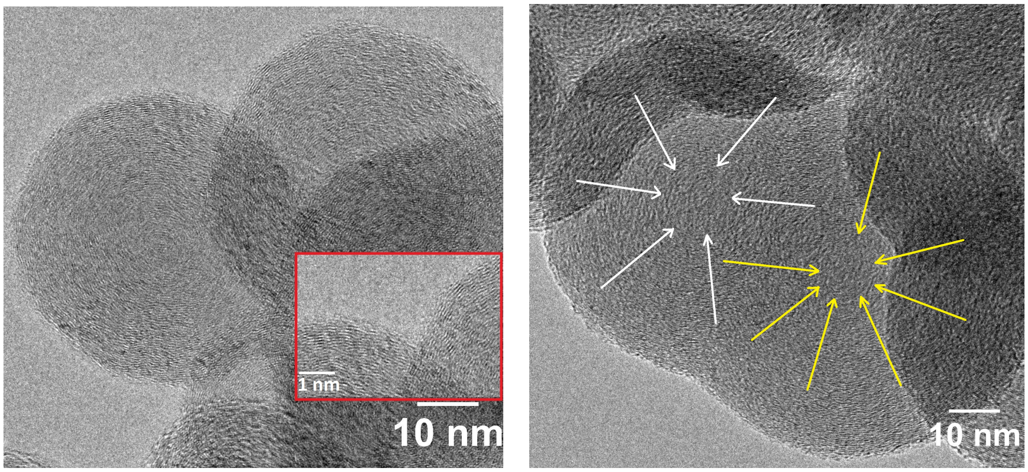

7(a): Pinewood soot (1250°C)

7(b): Multi-cores of pinewood soot (1250°C)

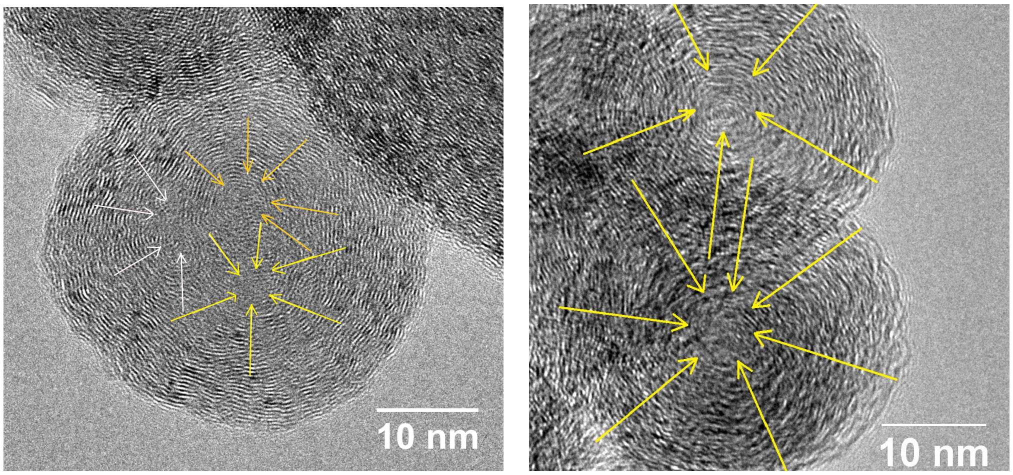

7(c): Beechwood soot (1400°C)

7(d): Wheat straw soot (1250°C)

Figure 7: TEM images of soot generated from (a)-(b) pinewood (1250°C), (c) beechwood (1400°C) and (d) wheat straw (1250°C). In Figure (a) the distance between graphene layers is enlarged using the red rectangle. In Figures (b)-(d) the arrows show the multiple cores of soot particles.

Compared to the pinewood soot produced at 1250°C, the beechwood soot particles were located closer to each other due to the particle coalescence at an earlier stage. Liati et al.[16] related the multi-core structure to an early phase of soot formation by nuclei coalescence and further development as a single particle. The multi-core structure of pinewood soot produced at 1250°C reflects formation by coalescence of several smaller particles, with this process governed by the particle concentration, as suggested by Lee et al. [85]. Due to the highest soot yield at 1250°C and the ability of pinewood to generate more soot compared to beechwood and wheat straw, the primary soot particles probably coalesced with other soot particles forming multi-core structures. Both fine and large primary soot particles consisted of monolayers of graphene sheets, which grow circumferentially from the particle core. The shell of small particles provided a clear fringe contrast from the stacking of the graphene layers, which is less obvious for larger particles due to their thickness (supplementary Figure S-3). This limitation also applied to the core of the larger particles, which characterization was not possible. Still, the shell nanostructure of smaller and larger particles seems to be similar as shown in Figure 7 and in supplementary Figures S-2 and S-3.

Figure 7 shows that the particle cores consist mainly of randomly orientated and curved graphene layers. Su et al. [86] investigated the reactivity of soot formed in the exhaust from diesel engine with respect to oxidation, and described a soot core as a highly reactive area of a soot particle due to the defects on the surface being functionalized with volatile groups. They hypothesized that the defective non-6-membered rings may produce highly localized olefinic electronic structures in the soot core that are prone to oxidation.

All soot samples exhibited a well-ordered graphitic structure. The graphene segments of the samples were mainly placed parallel to each other, and were relatively straight with the smaller curvature of an average particle size (flat graphene ≈1 [14]) as shown in Table 5.

Table 5: Summary of soot characteristics (cure, curvature, separation distance) prepared from pinewood, beechwood and wheat straw pyrolysis at 1250 and 1400°C. Standard deviation was calculated for curvature and separation distance.

Soot	**1250°C**				**1400°C**			
	Fiber length	Curvature^2	$d_{sep}{}^{1,2}$	Core^{3,4}	Fiber length	Curvature^2	$d_{sep}{}^{1,2}$	Core^{3,4}
	nm		nm		nm		nm	
Pinewood	2±0.8	0.88±0.02	0.33±0.01	mostly m	2.2±0.9	0.88±0.02	0.34±0.02	m & s
Beechwood	3.1±1.1	0.88±0.02	0.35±0.02	m & s	3.2±1.2	0.88±0.02	0.35±0.02	m & s
Wheat straw	2.7±0.9	0.85±0.05	0.35±0.02	s	2.6±1	0.86±0.05	0.35±0.02	s

[1] Separation distance

[2] Calculation of mean curvature and d_{sep} of graphene layers measured only on crystallites

[3,4] *s* - single core and *m* - multiple cores

Table 5 summarizes the characteristics of different soot samples with regards to single or/and multiple cores, curvature and separation distance of graphene layers. The mean separation distance of woody and herbaceous soot graphene segments was measured to be < 0.35 nm, which is similar to the layer distance determined by X-ray diffraction.

3.6. TEM-EELS Measurements

The carbon core-loss edge (C-K edge) at about 285 eV was recorded under magic-angle conditions to reduce the possible influence of anisotropy of the sample [47, 87]. Figure 8 shows the EELS spectra of graphite tilted in two different directions, verifying magic-angle conditions. The spectra were collected in diffraction mode. Due to limitation of the selected area diffraction aperture, agglomerates of typical 1-7 soot particles of different sizes were probed, with a total of 15-20 agglomerates per soot sample prepared at 1400°C.

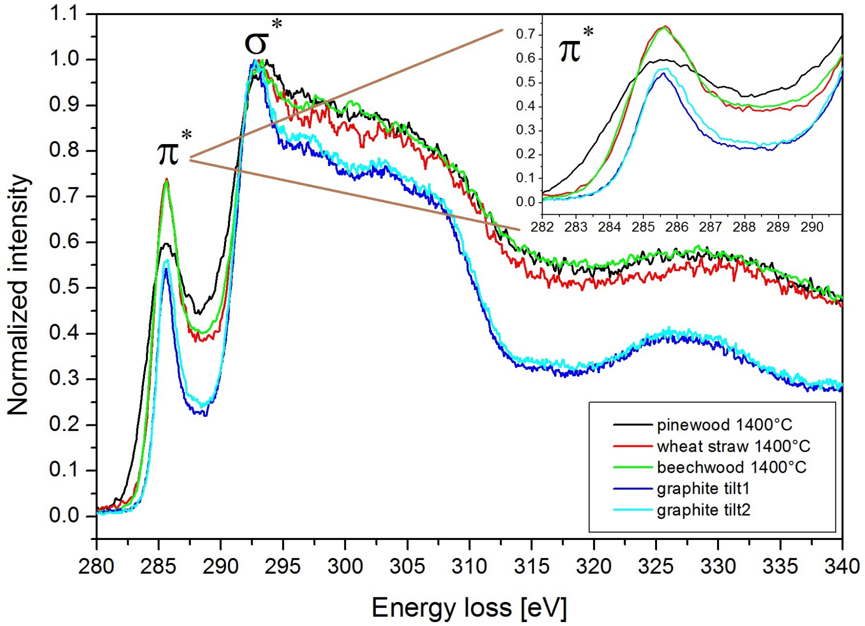

Figure 8: TEM-EELS averaged spectra of pinewood, beechwood and wheat straw soot samples (1400°C) which are shown by black, green and red lines. TEM-EELS spectra of graphite is shown by cyan and blue lines. The graphite was tilted in two different directions to verify magic-angle conditions. Maxima of 1 s-π^* and 1 s-σ^* transitions were illustrated by π^* and σ^* symbols.

The C-K edge showed mainly two distinct maxima, one at about 285 eV of 1 s-π^* transitions, which was attributed to C=C bonds (sp^2 hybridization), and a second at about 292 eV of 1 s-σ^* transitions, attributed to C-C bonds (sp^3 hybridization) as shown in Figure 8. To quantify the amount of sp^2/sp^3 hybridized carbon and to compare the samples, the two peaks were fitted by individual Gaussian peaks. The ratio of the area under the Gaussian curves, $r = A_{G,\pi*} / A_{G,\sigma*}$, gave an indication about the sp^2/sp^3 ratio in the probed volume (supplementary Figure S-5). A defect-free clean graphite should give a ratio of about 0.33. From the manual fitting of these two peaks of the measured graphite a ratio of about 0.24 was calculated. This could be due to defects or amorphous carbon contamination, which reduced the amount of sp^2 hybridized carbon and increased the amount of sp^3 carbon. From the fit (supplementary Figure S-5) it was obvious that these two peaks did fully resemble the spectra in this energy region. Additional intensity was required between 287 and 289 eV, presumably due to non-carbon-carbon bonding [14, 88–91]. The ratio for all three soot samples was higher than for pure graphite, 0.28-0.36 [92]. As graphite is the material with the highest sp^2/sp^3 ratio, this indicate that fewer sp^3 carbon-carbon bonds were present in soot. This is in agreement with the visible nanostructure, indicating defective graphene flakes, which were probably terminated by for example C-H bonds. The present EELS data suggest a structure closer to graphite for wheat straw and beechwood soot than for pinewood soot. The spectra of individual agglomerates within one sample showed no significant differences. No obvious particle size dependence of the spectra was observed.

An O-K edge was present in the EELS spectra of several wheat straw soot agglomerates. No oxygen edge was detected for pinewood and beechwood soot. Additionally, beechwood and wheat straw soot showed two additional peaks at about 298 eV and 300.5 eV for several agglomerates, which were assigned to the K-$L_{2,3}$ edge of potassium. In wheat straw soot both, the oxygen and potassium edge were detected for the same agglomerates.

4. Discussion

The thermogravimetric experiments demonstrated significant differences in the reactivity of pinewood, beechwood and wheat straw soot towards O_2 and CO_2. The reaction rate measured by TG instrument was mainly limited by chemical kinetics, while the importance of diffusion limitations, calculated under the assumption of reaction taking place on the outer surface of non-porous soot particles (supplementary Table S-6) was small. The oxidation of the beechwood and wheat straw soot prepared at 1250 and 1400°C took place at nearly the same temperature range, whereas the maximum reaction rate of pinewood soot was shifted to higher temperatures, indicating a lower reactivity. Woody and herbaceous soot samples prepared at 1250°C were less reactive than soot produced at 1400°C at both oxidation and CO_2 gasification conditions.

The reactivity of soot samples can be affected by the differences in alkali content, particle size and soot nanostructure. Liati et al. [16] reported that soot nanostructure may affect the oxidation reactivity. Low separation distances (close to that of graphite) and high periodicity lead to lower oxidation of soot, while the more bent graphene layers might enhance the reactivity. The EELS analysis showed that the nanostructure of beechwood and wheat straw soot was more similar to graphite compared to the nanostructure of pinewood soot. Thus, based on structure alone it might be expected that pinewood soot should be reactive than the soot from beechwood and straw.

However, it was observed that the low-ash containing pinewood soot prepared at 1250 and 1400°C was 143 and 571 times less reactive than the alkali rich wheat straw soot in CO_2 gasification. Significantly smaller differences in CO_2 reactivity were observed for the beechwood soot prepared at 1250 and 1400°C compared to pinewood soot (8 and 35 times), respectively. The particle size of wheat straw soot at 1250°C was two times smaller than pinewood soot, whereas the reaction rate of wheat straw soot was 143 times higher than pinewood soot as shown in Table 2. This indicates that neither soot structure nor particle size had a stronger influence on the observed differences in soot reactivity. In addition, the differences in nanostructure of pinewood, beechwood and wheat straw soot were small compared to that of soot prepared by pyrolysis of acetylene and benzene, where the formation conditions have significantly more influence on the soot nanostructure [11].

The results show that it is the presence of potassium in beechwood and wheat straw soot which mainly affects the reactivity during CO_2 gasification. Based on the TEM EELS, XRD and FTIR analysis results and equilibrium calculations with Factsage it was concluded that the potassium species were incorporated in the wheat straw soot particles mostly as KOH, KCl, $KHCO_3$ and K_2CO_3 and to a minor extent bonded in the soot matrix to the oxygen-containing surface groups. In beechwood soot, potassium was likely intercalated in the graphene layers because the oxygen content was below the detection limit of the TEM EELS and elemental analysis. The removal of water-soluble potassium from wheat straw soot by leaching led to a lower reactivity in CO_2 gasification at 1250 and 1400°C (by factors of 2.5 and 8, respectively). Furthermore, the activation energy of leached wheat straw soot was higher than that of non-treated wheat straw soot samples, indicating loss of catalytic activity by potassium removal. The leaching of beechwood soot did not, however, influence its reactivity. The potassium content of beechwood soot was lower than for wheat straw soot, and the major part was likely bonded to sites from which it was difficult to wash out (e.g. intercalated or in phenolates etc). Even after leaching, the reactivity of straw and beechwood soot was higher than that of pinewood soot. For example, the rate constants of leached wheat straw prepared at 1250 and 1400°C were 57 and 25 times higher than pinewood soot which has a very low potassium content and shown in Table 2. This indicates that potassium has a dominant role on the soot reactivity and that both potassium deposited on the surface particles and potassium incorporated into the soot matrix can influence the reactivity. In addition, the reaction rates (0.01 and $0.02\,s^{-1}$) of potassium impregnated graphite with 20 % and 30 % KNO_3 and the reaction rates (0.01 and $0.04\,s^{-1}$) of wheat straw soot prepared at 1250 and 1400°C were of the same order of magnitude in CO_2 gasification, indicating the reactivity increase by graphite impregnation with potassium.

The observation made by Qin et al. [5] and Septien et el. [33] in terms of the increasing soot reactivity with increased heat treatment temperatures was confirmed in the present study. The reaction rate of pinewood, beechwood and wheat straw soot generated at 1400°C was 4, 12 and 3 times higher than the reactivity of soot prepared at 1250°C. The specific surface area of pinewood soot prepared at 1400°C was significantly larger (by 1.6, 1.2 and 1.4 times) than that of soot generated at 1250°C. The results showed that the reaction rates of woody and herbaceous biomass soot at both temperatures increased faster than the soot surface area increased. This shows that another more dominating factor, i.e., the potassium content, affects the differences in reactivity in O_2 and CO_2 gasification.

5. Conclusion

Fast pyrolysis of pinewood, beechwood and wheat straw was conducted in a drop tube reactor to study the effect of biomass type on the yield, nanostructure and reactivity of soot at high temperatures. The soot yields from pinewood pyrolysis at 1250 and 1400°C were the highest (8.4 % and 6.7 wt. % daf), whereas the wheat straw soot yields were the lowest (2.5 and 2.7 wt. % daf).

The major difference in the soot morphology was related to the formation of irregular-shaped pinewood soot particles with mostly multiple cores, whereas beechwood and wheat straw soot samples were mainly single core structures at both investigated temperatures. Minor differences in particle size were also observed. Larger soot particles were formed by pyrolysis of pinewood at 1250°C as to soot generated at 1400°C and beechwood and wheat straw soot prepared at both temperatures. The particle size distribution of pinewood soot generated at 1250°C was significantly broader (from 27 to 263 nm), compared to other soot samples. The differences in nanostructure of wood and wheat straw soot were small, except for presence of single and multiple cores.

The thermogravimetric analysis results showed that the soot reactivity towards O_2 and CO_2 depends mainly on the potassium content in the original fuel and on the heat treatment temperature and less on the soot nanostructure. For fuels with a high potassium content, there will be higher potassium release to the gas phase in the temperature range from 1250 to 1400°C, and so more potassium incorporates in the soot particles. The temperature (1250 or 1400°C) at which soot was formed therefore affects strongly the soot reactivity in CO_2 gasification and to a minor extent at oxidation conditions. The pinewood soot was less reactive than beechwood and wheat straw soot generated under similar operating conditions due to the low potassium content of the original pinewood, despite the pinewood soot having a less graphitic structure. The potassium was present both as water-soluble alkali and incorporated with the oxygen containing surface groups in the soot matrix and both contributed to the higher reactivity of beechwood and wheat straw soot in CO_2 gasification.

Acknowledgements

The authors at DTU would like to acknowledge the financial support that they received for this project from Danish Strategic Research Council (Grant Nr. DSF-10-093956), DONG Energy and Vattenfall. We also thank Professor Kenny Ståhl (DTU Chemistry) for assisting with XRD measurements and data processing and Professor Søren Talbro Barsberg (University of Copenhagen) for assisting with FTIR measurements. The A.P. Møller and Chastine Mc-Kinney Møller Foundation is acknowledged for their contribution toward the establishment of the Center for Electron Nanoscopy in the Technical University of Denmark and thanks to Wilhelmus Huyzer for initial TEM imaging. Assistant Professor Catherine Brewer is acknowledged for the article proof reading. The authors acknowledge Professor Randy Vander Wal

for the scientific discussions.

References

[1] Puig-Arnavat M, Soprani S, Søgaard M, Engelbrecht K, Ahrenfeldt J, Henriksen UB, Hendriksen PV, Integration of mixed conducting membranes in an oxygen-steam biomass gasification process, RSC Adv 3 (2013) 20843–54.

[2] Qin K, Lin W, Jensen PA, Jensen AD, High-temperature entrained flow gasification of biomass, Fuel 93 (2012) 589–600.

[3] Septien S, Valin S, Peyrot M, Dupont C, Salvador S, Characterization of char and soot from millimetric wood particles pyrolysis in a drop tube reactor between 800°C and 1400°C, Fuel 121 (2014) 216–24.

[4] Wilson JM, Baeza-Romero MT, Jones JM, Pourkashanian M, Williams A, Lea-Langton AR et al., Soot Formation from the Combustion of Biomass Pyrolysis Products and a Hydrocarbon Fuel, n-Decane: An Aerosol Time of Flight Mass Spectrometer (ATOFMS) Study, Energy Fuels 27 (3) (2013) 1668–78.

[5] Qin K, Lin W, Fœster S, Jensen PA, Wu H, Jensen AD, Characterization of Residual Particulates from Biomass Entrained Flow Gasification, Energy Fuels 27 (1) (2013) 262–70.

[6] Alonso MJG, Borrego AG, Alvarez D, Meneendez R, Pyrolysis behaviour of pulverised coals at different temperatures, Fuel 78 (13) (1999) 1501–13.

[7] Chen J, Effect of Secondary Reactions on Product Distribution and Nitrogen Evolution From Rapid Coal Pyrolysis. PhD thesis, Stanford University (1991).

[8] Bilbao R, Millera A, Alzueta MU, Influence of the Temperature and Oxygen Concentration on NO_x Reduction in the Natural Gas Reburning Process, Ind Eng Chem Res 33 (11) (1994) 2846–52.

[9] Sanchez NE, Callejas A, Millera A, Bilbao R, Alzueta MA, Determination of Polycyclic Aromatic Hydrocarbons (PAH) Adsorbed on Soot Formed in Pyrolysis of Acetylene at Different Temperatures, Chem Eng Trans 22 (2010) 131–6.

[10] Vander Wal RL, Tomasek AJ, Soot oxidation: dependence upon initial nanostructure, Combust Flame 134 (1-2) (2003) 1–9.

[11] Vander Wal RL, Tomasek AJ, Soot nanostructure: dependence upon synthesis conditions, Combust Flame 136 (1-2) (2004) 129–40.

[12] Roth K, Soot formation during the production of syngas from the partial oxidation of diesel fuel. PhD thesis, Ruhr University of Bochum (2006).

[13] Le Manquais K, Snape C, Barker J, McRobbie I, TGA and Drop Tube Furnace Investigation of Alkali and Alkaline Earth Metal Compounds as Coal Combustion Additives, Energy Fuels 26 (3) (2012) 1531–9.

[14] Müller JO, Su DS, Wild U, Schlögl R, Bulk and surface structural investigations of diesel engine soot and carbon black, Phys Chem Chem Phys 9 (2007) 4018–25.

[15] Müller JO, Frank B, Jentoft RE, Schlögl R, Su DS, The oxidation of soot particulate in the presence of NO_2, Catal today 191 (1) (2012) 106–11.

[16] Liati A, Eggenschwiler PD, Schreiber D, Zelenay V, Ammann M, Variations in diesel soot reactivity along the exhaust after-treatment system, based on the morphology and nanostructure of primary soot particles, Combust Flame 160 (3) (2013) 671–81.

[17] van Setten B, Makkee M, Moulijn JA, Science and technology of catalytic diesel particles oxidation, Catal Sci Rev Eng 43 (2001) 489–564.

[18] Wen YW, Mechanisms of Alkali Metal Catalysis in the Gasification of Coal, Char, or Graphite, Cat Rev Sci Eng 22 (1) (1980) 1–28.

[19] Moulijn JA, Kapteijn F, Towards a unified theory of reactions of carbon with oxygen-containing molecules, Carbon 33 (8) (1995) 1155–65.

[20] Chen SG, Yang RT, The Active Surface in Alkali-Catalyzed Carbon Gasification: Phenolate (C-O-M) Groups vs Clusters (Particles), J Catal 141 (1) (1993) 102–13.

[21] Mul G, Kapteijn F, Moulijn JA, Drift analysis of surface oxygen complexes on soot formed by metal oxides, ACS Div Fuel Chem 41 (1) (1996) 230–4.

[22] Kröger C, Die Vergasung von Kohlenstoff durch Luft, Kohlendioxyd und Wasserdampf und ihre Beeinflussung durch anorganische Katalysatoren, Angewandte Chemie 52 (6) (1939) 129–39.

[23] Walker PL, Shelef M, Anderson RA, Catalysis of Carbon Gasification, Marcel Dekker, 1968.

[24] Neeft PA, Makkee M, Moulijn JA, Catalysts for the oxidation of soot from diesel exhaust gases. I. An exploratory study, Appl Catal B: Environ 8 (1) (1996) 57–78.

[25] Neeft PA, Makkee M, Moulijn JA, Catalytic oxidation of carbon black - I. Activity of catalysts and classification of oxidation profiles, Fuel 77 (3) (1998) 111–9.

[26] Miro EE, Ravelli F, Ulla MA, Cornaglia LM, Querini CA, Catalytic combustion of diesel soot on Co, K supported catalysts, Catal Today 53 (4) (1999) 631–8.

[27] Serra V, Saracco G, Badini C, Specchia V, Combustion of carbonaceous materials by Cu-K-V based catalysts: II. Reaction mechanism, Appl Catal B 11 (1997) 329–46.

[28] Fredenhagen K, Cadenbach G, The formation of kalium through carbon, Zeitschrift fur Anorganische und Allgemeine Chemie 158 (1) (1926) 249–63.

[29] Fredenhagen K, Suck H, Regarding the bonding of the alkali metals through carbon, Zeitschrift fur Anorganische und Allgemeine Chemie 178 (4) (1929) 353–65.

[30] Fitzpatrick EM, Bartle KD, Kubacki ML, Jones JM, Pourkashanian M, Ross AB et al., The mechanism of the formation of soot and other

pollutants during the co-firing of coal and pine wood in a fixed bed combustor, Fuel 88 (12) (2009) 2409–17.

[31] Jones JM, Ross AB, Williams A, Short communication - Atmospheric chemistry implications of the emission of biomass smoke, J Eur Ceram Soc 78 (4) (2006) 199–200.

[32] Wiinikka H, Weiland F, Pettersson E, Öhrman O, Carlsson P, Characterisation of submicron particles produced during oxygen blown entrained flow gasification of biomass, Combust Flame 161 (7) (2014) 1923–34.

[33] Septien S, Valin S, Dupont C, Peyrot M, Salvador S, Effect of particle size and temperature on woody biomass fast pyrolysis at high temperature (1000-1400 °C), Fuel 97 (2012) 202–10.

[34] Göktepe B, Umeki K, Gebart R, Does distance among biomass particles affect soot formation in entrained flow gasification process?, Fuel Process Technol 141 (2016) 99–105.

[35] Umeki K, Kirtania K, Chen L, Bhattacharya S, Fuel Particle Conversion of Pulverized Biomass during Pyrolysis in an Entrained Flow Reactor, Ind Eng Chem Res 51 (43) (2012) 13973–9.

[36] Barsberg S, Thygesen LG, Sanadi AR, Control of Lignin Solubility and Particle Formation Modulates its Antioxidant Efficiency in Lipid Medium: An In Situ Attenuated Total Reflectance FT-IR Study, Environ Sci Technol 28 (2014) 4539–44.

[37] Warren BE, X-ray study of the graphitization of carbon black, Phys Rev 59 (1941) 693–8.

[38] Stenebråten JF, Johnson WP, McMullen J, Characterization of Goldstrike ore carbonaceous material, Miner Metall Process 17 (1) (2000) 7–15.

[39] Saikia BK, Boruah RK, Gogoi PK, A X-ray diffraction analysis on graphene layers of Assam coal, J Chem Sci 121 (1) (2009) 103–6.

[40] Zolin A, Jensen AD, Jensen PA, Dam-Johansen K, Experimental study of char thermal deactivation, Fuel 81 (8) (2002) 1065–75.

[41] Septien Stringel S, High temperature gasification of millimetric wood particles between 800°C and 1400°C. PhD thesis, RAPSODEE (Ecole des Mines d'Albi-Carmaux) (2011).

[42] Abian M, Jensen AD, Glarborg P, Alzueta MU, Soot Reactivity in Conventional Combustion and Oxy-fuel Combustion Environments, Energy Fuels 26 (8) (2012) 5337–44.

[43] Coats AW, Redfern JP, Kinetic parameters from thermogravimetric data, Nature 201 (1964) 68–9.

[44] Brunauer S, Emmett PH, Teller E, Adsorption of Gases in Multimolecular Layers, J Am Chem Soc 60 (2) (1938) 309–19.

[45] Leapman RD, Fejes PL, Silcox J, Orientation dependence of core edges from anisotropic materials determined by inelastic scattering of fast electrons, Phys Rev B 28 (5) (1983) 2361–73.

[46] Pettifer RF, Brouder C, Benfatto M, Natoli CR, Magic-angle theorem in powder X-ray-absorption spectroscopy, Phys Rev B 42 (1) (1990) 37–42.

[47] Daniels H, Brown A, Scott A, Nichells T, Rand B, Brydson R, Experimental and theoretical evidence for the magic angle in transmission electron energy loss spectroscopy, Ultramicroscopy 96 (3-4) (2003) 523–34.

[48] Schattscheider P, Hebert C, Franco H, Anisotropic relativistic cross sections for inelastic electron scattering, and the magic angle, Phys Rev B 72 (4) (2005) 1–8.

[49] Hebert C, Schattschneider P, Franco H, Jouffrey B, ELNES at magic angle conditions, Ultramicroscopy 106 (11-12) (2006) 1139–43.

[50] Finlay WH, The Mechanics of Inhaled Pharmaceutical Aerosols. An Introduction, Academic Press, 2001.

[51] Russell NV, Beeley TJ, Man CK, Gibbins JR, Williamson J, Development of TG measurements of intrinsic char combustion reactivity for industrial and research purposes, Fuel Process Tech 57 (2) (1998) 113–30.

[52] Hirschon AS, Du Y, Wu HJ, Wilson RB, Malhotra R, Effect of Doping Fullerene Soots with Metals on the Conversion of Methane into Higher Hydrocarbons, Res Chem Intermed 23 (7) (1997) 675–82.

[53] Müller JO, Investigations on Environmental Carbons. PhD thesis, Technical University of Berlin (2012).

[54] Meijer R, Weeda M, Kapteijn F, Moulijn JA, Catalyst loss and retention during alkali-catalysed carbon gasification in CO_2, Carbon 29 (7) (1991) 929–41.

[55] McKee DW, Gasification of graphite in carbon dioxide and water vapor - the catalytic effects of alkali metal salts, Carbon 20 (1) (1982) 59–66.

[56] Decesari S, Facchini MC, Matta E, Mircea M, Fuzzi S, Chughtai AR et al., Water soluble organic compounds formed by oxidation of soot, Atmos Environ 36 (11) (2002) 1827–32.

[57] Takahama S, Liu S, Russell LM, Coatings and clusters of carboxylic acids in carbon-containing atmospheric particles from spectromicroscopy and their implications for cloud-nucleating and optical properties, J Geophys Research 115 (D1) (2010) 1–21.

[58] Bi H, Kou KC, Ostrikov K, Zhang JQ, Graphitization of nanocrystalline carbon microcoils synthesized by catalytic chemical vapor deposition, J Appl Phys 104 (3) (2008) 1–6.

[59] Blayden HE, Gibson J, Riley HL, An X-Ray Study of the Structure of Coals and Cokes, Proc British Coal Util Res Assoc (1944) 176–231.

[60] Roberts MJ, Everson RC, Neomagus NWJP, van Niekerk D, Mathews JP, Branken DJ, Influence of maceral composition on the structure, properties and behaviour of chars derived from South African coals, Fuel 142 (2015) 9–20.

[61] Belenkov EA, Formation of Graphite Structure in Carbon Crystallites, Inorg Mater 37 (9) (2001) 928–34.

[62] Marsh PA, Voet A, Mullens TJ, Price LD, Electron microscopy of interplanar spacing in carbon blacks. Proc Meeting ACS Div of Rubber Chem; 1969 October 14^{th}-17^{th}, Buffalo, NY, US, 470-80.

[63] Bockhorn H, D'Anna A, Sarofim AF, Wang H, Combustion Generated Fine Carbonaceous Particles, KIT Sci Publ, 2009.

[64] Trubetskaya A, Jensen PA, Garcia Llamas AD, Umeki K, Jensen AD, Glarborg P, Effect of fast pyrolysis conditions on biomass solid residues at high temperatures, Fuel Process Tech 143 (2016) 118–29.

[65] Knudsen JN, Jensen PA, Dam-Johansen K, Transformation and Release to the Gas Phase of Cl, K and S during Combustion of Annual Biomass, Energy Fuels 18 (2004) 1385–99.

[66] Dayton DC, Milne TA, Laboratory Measurements of Alkali Metal Containing Vapors Released during Biomass Combustion. In L. Baxter and R. DeSollar, Application of Advanced Technologies to Ash-Related Problems in Boilers, Plenum Press, 1996.

[67] Knudsen JN, Volatilization of Inorganic Matter during Combustion of Annual Biomass. PhD thesis, Technical University of Denmark (2003).

[68] Puri BR, Surface complexes on carbons, Chem Phys Carbon 6 (1970) 191–282.

[69] Puri BR, Hazra RS, Carbon-sulfur surface complexes on charcoal, Carbon 9 (1971) 123–34.

[70] Cal MP, Strickler BW, Lizzio AA, Gangwal SK, High temperature hydrogen sulfide adsorption on activated carbon - II. Effects of gas temperature, gas pressure and sorbent regeneration, Carbon 38 (2000) 1767–74.

[71] Guenzler H, Boeck H, IR-Spektroskopie. Eine Einführung, Verlag Chemie and Physik, 1983.

[72] Reddy BVR, Chakrapani C, Babu CS, Rao KS, Agarwal K, Prasad M, FT-IR, TG, XRD and SEM Studies of Activated Carbons Prepared from Agricultural Waste, Asian J Chem 22 (3) (2010) 1822–8.

[73] Zhang Z, Zhang Y, Su Q, Wang Z, Li Q, Gao X, Determination of Intermediates and Mechanism for Soot Combustion with NO_x/O_2 on Potassium-Supported Mg-Al Hydrotalcite Mixed Oxides by In Situ FTIR, Environ Sci Technol 44 (21) (2010) 8254–8.

[74] Philipp R, Omata K, Aoki A, Fujimoto K, On the active site of MgO/CaO mixed oxide for oxidative coupling of methane, J Catal 134 (1992) 422–33.

[75] Legutko P, Jakubel T, Kaspera W, Stelmachowski P, Sojka Z, Kotarba A, Soot oxidation over K-doped manganese and iron spinels - How potassium precursor nature and doping level change the catalyst activity, Catal Commun 43 (2014) 34–7.

[76] Gu B, Schmitt J, Chen Z, Liang L, McCathy JF, Adsorption and Desorption of Natural Organic Matter on Iron Oxide: Mechanisms and Models, Environ Sci Technol 28 (1) (1994) 38–46.

[77] Ibrahim M, Nada A, Kamal DE, Density functional theory and FTIR spectroscopic study of carboxyl group, Indian J Pure Appl Phys 43 (12) (2005) 911–7.

[78] Akuzawa N, Yoshioka J, Ozaki C, Tokuda M, Ohkura K, Soneda Y, Preparation and characterization of sodium-graphite intercalation compounds, Mol Cryst Liq Cryst 388 (1) (2002) 1–7.

[79] Chakrabarty RK, Moosmüller H, Garro MA, Arnott WP, Walker J, Susott RA et al., Emissions from the laboratory combustion of wildland fuels: Particle morphology and size, J Geophys Research 111 (D7) (2006) 1–16.

[80] Sachdeva K, Attri AK, Morphological characterization of carbonaceous aggregates in soot and free fall aerosol samples, Atmos Environ 42 (5) (2008) 1025–34.

[81] Ross AB, Junyapoon S, Jones JM, Williams A, Bartle KD, A study of different soots using pyrolysis-GC-MS and comparison with solvent extractable material, J Anal Appl Pyrolysis 74 (2005) 494–501.

[82] Posfai M, Simonics R, Hobbs PV, Buseck PR, Individual aerosol particles from biomass burning in Southern Africa: 1. Composition and size distributions of carbonaceous particles, J Geophys Res Atmos 108 (D13) (2003) 1–20.

[83] Posfai M, Gelencser A, Simonics R, Li J, Hobbs PV, Buseck PR, Atmospheric tar balls: Particles from biomass and biofuel burning, J Geophys Res 109 (D6) (2003) 1–9.

[84] Arora P, Jain S, Morphological characteristics of particles emitted from combustion of different fuels in improved and traditional cookstoves, J Aerosol Sci 82 (2015) 13–23.

[85] Lee KO, Cole R, Sekar R, Kang J, Bae C, Zhu J, Detailed Characterization of Morphology and Dimensions of Diesel Particulates via Thermophoretic Sampling, Sae Tech Papers (2001) 1–10.

[86] Su DS, Müller JO, Jentoft RE, Rothe D, Jacob E, Schlögl R, Fullerene-like Soot from EURO-IV Diesel Engine: Consequences for Catalytic Automotive Pollution Control, Topics in Catal 30 (31) (2004) 241–5.

[87] Loretto MH, Electron beam analysis of materials, Chapman & Hall, 1994.

[88] Papworth AJ, Kiely CJ, Burden AP, Silva SRP, Amaratunga GAJ, Electron-energy-loss spectroscopy characterization of the sp^2 bonding fraction within carbon thin films, Phys Rev B 62 (2000) 628–31.

[89] Brauns A, Huggins FE, Shah N, Chen Y, Wirick S, Mun SB, Advantages of soft X-ray absorption over TEM-EELS for solid carbon studies - a comparative study on diesel soot with EELS and NEXAFS, Carbon 43 (1) (2005) 117–24.

[90] Mackovic M, Characterization of soot particles from diesel engines and tin dioxide particles milled in stirred media mills. PhD thesis. University of Erlangen-Nürnberg (2012).

[91] Cohen-Ofri I, Popovitz-Biro R, Weiner S, Structural characterization of modern and fossilized charcoal produced in natural fires as determined

by using electron energy loss spectroscopy, Chem Eur J 13 (8) (2007) 2306–10.

[92] Berndt F, Kleebe HJ, Ziegler G, Evidence for Structural Changes of Amorphous Carbon Coatings on Silicon Carbide During Tribological Tests, J Am Ceram Soc 82 (11) (1999) 3161–6.